

Article

Electrical Performance Compensation of Reflector Antenna Based on Sub-Reflector Array

Jie Zhang ^{1,*}, Xiangpeng Kong ², Chuyun Zhang ² , Yifan Gao ² and Qiang He ²

¹ State Key Laboratory of Electromechanical Integrated Manufacturing of High-Performance Electronic Equipments, Xidian University, Xi'an 710126, China

² School of Mechano-Electronic Engineering, Xidian University, Xi'an 710126, China; 20041212052@stu.xidian.edu.cn (X.K.); chuyunzhang@stu.xidian.edu.cn (C.Z.); 21041212144@stu.xidian.edu.cn (Y.G.); 21181214517@stu.xidian.edu.cn (Q.H.)

* Correspondence: jiezhang1987@xidian.edu.cn

Abstract: Large high-frequency reflector antennas typically operate outdoors and are impacted by environmental factors such as wind, rain, snow, solar radiation, etc. These conditions cause the antenna structures to distort, which, in turn, affects electrical performance. The observation performance of the antenna is seriously affected. To solve this problem, based on the active control of sub-reflector arrays, an optimization method for sub-reflector arrays and an active compensation method for electrical performance are proposed. Through real-time regulation of the phase plane of the distorted aperture field, the electrical performance of the antenna can be compensated for. The research object, a 65 m Cassegrain dual-reflector antenna, is designed in this work using a sub-reflector with an aperture of 6.1 m. The form and posture of the sub-reflector are comprehensively changed by adjusting the position of the sub-reflector panel and the overall movement of the sub-reflector, and the phase inaccuracy of the aperture field brought by the deformation of the main reflector is compensated for. The simulation results demonstrate that the maximum gain loss can be reduced from 0.44315 dB to 0.0803 dB and the maximum point error can be reduced from 0.00143° to 0.00047° under wind load with an average wind speed of 12 m/s using the active sub-reflector array adjustment strategy proposed.

Keywords: dual-reflector antenna; electrical performance compensation; sub-reflector array



Citation: Zhang, J.; Kong, X.; Zhang, C.; Gao, Y.; He, Q. Electrical Performance Compensation of Reflector Antenna Based on Sub-Reflector Array. *Electronics* **2023**, *12*, 4771. <https://doi.org/10.3390/electronics12234771>

Academic Editor: Naser Ojaroudi Parchin

Received: 10 October 2023
Revised: 13 November 2023
Accepted: 20 November 2023
Published: 24 November 2023



Copyright: © 2023 by the authors. Licensee MDPI, Basel, Switzerland. This article is an open access article distributed under the terms and conditions of the Creative Commons Attribution (CC BY) license (<https://creativecommons.org/licenses/by/4.0/>).

1. Introduction

1.1. Background

As big reflector antennas with huge apertures and high-frequency bands are increasingly being developed, the electrical performance of the antenna—such as gain and pointing accuracy—becomes more crucial. However, when the antenna's aperture grows, its structural stiffness reduces, leading to a greater amount of structural deformation. For instance, when a 110 m aperture antenna is oriented at 90°, the reflector introduces a 1.126 mm surface error because of gravity, which results in a gain loss of 2.367 dB and a 17.9 arcsecond deviation of the beam direction. This is significantly below the pointing accuracy index's 1.5 arcsecond cutoff [1]. A temperature gradient load of 7.8 °C applied to a reflector for a 35 m aperture antenna causes a gain loss of 0.323 dB and a pointing deviation of 0.005° [2]. The electric performance loss induced by the environmental load, such as gain loss and pointing error, will shorten the observation distance and reduce the observation efficiency of the antenna.

This paper presents a solution to this issue by suggesting an electrical performance-oriented chunked sub-face design method and an active compensation method that actively modify the chunked sub-face's shape and attitude to make up for the electrical performance loss. Simulation is used to verify the compensation method's viability.

This approach has the advantages of being simple to adjust and easy to implement, and having high adjustment accuracy by chunking the sub-face when compared to the classic main face compensation, sub-face attitude compensation, and flexible sub-face shape compensation methods according to the literature.

1.2. Research Status at Home and Abroad

Academics have proposed a variety of compensating strategies to solve the problem of electrical performance loss caused by the deformation of large reflector antennas under environmental stress. One of the most often utilized approaches is electrical performance compensation based on active reflector adjustment technology. It is shown in [3] that the gain loss is related to the dimensional accuracy of the reflector. Therefore, the forming accuracy of the reflector needs to be improved to compensate for the gain loss brought on by the deformation of the reflective surface. There is now active adjustment technology. By changing the shape of the antenna's primary reflector, this technique offsets the deformation of the main reflector brought on by the environmental load. The first active reflector antenna was created in the United States in 1999 [4]. The accuracy of the reflector was increased to 0.24 mm after using active reflector compensation. Wang proposed a method for calculating the panel adjustment of a distorted paraboloid antenna for gain and pointing by using the best-fitting reflector as the reference surface and combining it with the drive stroke minimization according to the requirements of the antenna's electrical performance. The loss of electric performance brought on by the structural deformation of an antenna is compensated for through the active adjustment of the panel [1]. Even though active reflector technology increases the antenna's accuracy under environmental pressures, the antenna requires several actuators, making coordination challenging and the control system intricate. The only acceptable variables are quasi-static ones like temperature and gravity.

Gawronski used a PID control algorithm and a control algorithm to correct for angle error through an antenna servo system for a pointing error compensation method based on servo control [5]. Zhang created a pointing control-oriented model (PCOM) and devised an LQG controller based on it, with the goal of the real-time estimation and correction of structural flexible deformation brought on by the wind. Using this model, the maximum pointing error was reduced to 23% of the conventional PID controller [6]. Jie Zhang created a configuration of an active control beam waveguide with a real-time position adjustable plate mirror (APM) to lessen the pointing inaccuracy of an antenna under random wind load. Through inverse displacement analysis, the pointing errors resulting from reflector surface distortions were compensated for by properly adjusting the position of the APM [7]. Although it can correct wind disturbance, the antenna servo system is unable to correct the phase error of the aperture field brought on by reflector deformation.

In addition to the above compensation methods, some scholars compensate for the loss of electrical performance by changing the position of the sub-reflector. Wang [8] determined the ideal position of the sub-reflector corresponding to the distorted main plane to address the issue of poor electrical performance brought on by the deformation of the main plane of a Cassegrain antenna. The main reflector deformation can be corrected in real time by saving the sub-reflector location of each operating condition in the database. To account for antenna deformation, Ban [9] examined the reflector antenna's far-field mode and suggested a PEIC-based sub-reflector position adjustment approach. PEIC is a correction design method for the iterative compensation of optical range differences. Through the iterative design process, it is possible to obtain a corrected sub-reflector surface shape that plays a compensating role. This strategy, however, does not account for the gain loss brought on by the reflector's localized distortion. A novel antenna form using a planar reflector array instead of a hyperbolic sub-reflector was proposed [10]. Rahmat-Samii proposed using a reflector array as the sub-reflector for a large reflector antenna, utilizing the phase compensation function of the reflector array to compensate for the reflector deformation error caused by the gravity or temperature of large reflector antennas [11]. A new shape adjustment method for a sub-reflector was proposed to compensate for antenna

structural deformation, using actuators to minimize the residual wavefront error, and was verified to be effective under different elevation angles [12]. However, the method of using electric compensation has a limited effect on large deformation compensation. To further improve electrical performance, it is necessary to compensate for the shape distortion of the reflector.

2. Sub-Reflector Array Optimization

2.1. Influence of Environmental Load on Antenna's Aperture Field

A geometric diagram of the dual-reflector antenna is shown in Figure 1. In this figure, θ_f is the angle between the Z-axis and the reflected electromagnetic wave from the feed, and θ_p is an angle between the main surface and the Z-axis after the reflection of the electromagnetic wave emitted by the sub-reflector.

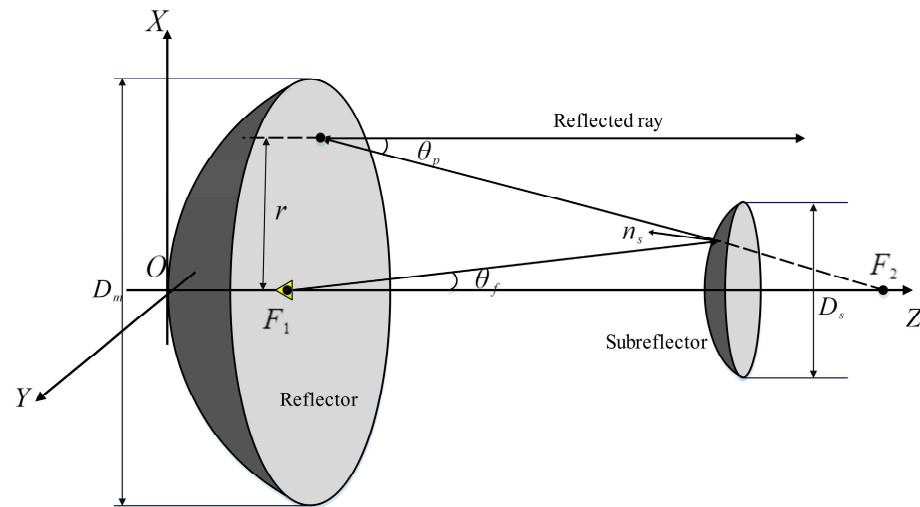


Figure 1. Geometric sketch of dual-reflector antenna.

Suppose a point x_m on the main plane deforms, and the surface error is $\delta_m = [\Delta x_p, \Delta y_p, \Delta z_p]^T$. The aperture surface optical path difference caused by surface error is as follows:

$$\delta_p = 2 \cdot (\Delta x_p \cos \alpha + \Delta y_p \cos \beta + \Delta z_p \cos \gamma) \cdot \cos \gamma \tag{1}$$

where $\alpha = \arctan(\frac{y}{x})$, $\cos \beta = \sin \alpha$, $\cos \gamma = \cos(\frac{\theta_p}{2})$, $\theta_p = 2\arctan(\frac{r}{2f})$, $\theta_f = 2\arctan(\frac{r}{2Mf})$, and $r = \sqrt{x^2 + y^2}$, where f is the focal length of the main plane, and M is the magnification of the antenna.

The sub-reflector shape distortion will lead to an aperture surface optical path difference, as shown in Figure 2. The deformation of the subsurface changes the point $K_0(x_0, y_0, z_0)$ to the point $K_0'(x_0', y_0', z_0')$ on the ideal hyperboloid, so the optical path difference is $S_1 + S_2$.

When the sub-reflector is deformed, assuming that the deformation distance of the sub-reflector shape is Δdn , the optical path difference generated is as follows:

$$\delta_s = S_1 + S_2 = S_1 + S_1 \cdot \cos 2\beta = 2S_1 \cdot \cos^2 \beta = 2\Delta dn \cdot \cos \beta \tag{2}$$

where Δdn is the normal displacement of the sub-reflector, β is half of the angle between incident rays and the reflected light. The relationship between the optical path difference and the distance of a point on the sub-reflector is as follows:

$$\Delta dn = \frac{\delta_s}{2 \cdot \cos \beta} \tag{3}$$

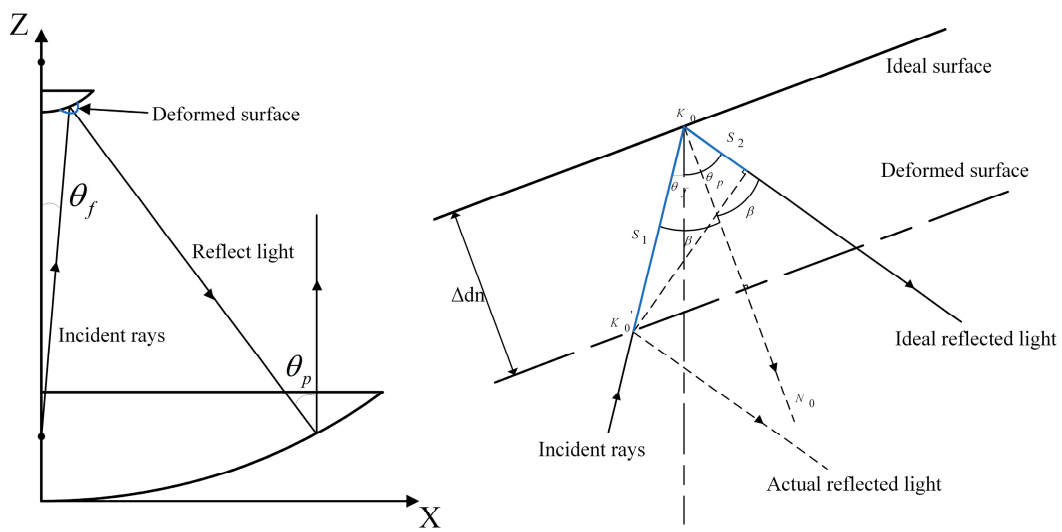


Figure 2. The change in optical path difference is caused by the deformation of the sub-reflector.

2.2. Determining the Error Compensation Interval

A flexible dynamic model is introduced to describe the deformation of the antenna. In this section, the modal superposition method is used to construct the flexible dynamic model of the antenna. Assuming that the main plane of the antenna contains n nodes, the dynamic model of the antenna in generalized coordinates [13] is:

$$\begin{aligned} \ddot{q}_m + 2Z\Omega\dot{q}_m + \Omega^2q_m &= B_m u \\ y &= C_{mq}q_m \end{aligned} \tag{4}$$

where Ω is a natural frequency matrix, a diagonal matrix composed of natural frequencies; Z is a modal damping matrix; and B_m and C_{mq} are the modal input matrix and modal output matrix, respectively. They are obtained as follows:

$$\begin{aligned} Z &= 0.5M_m^{-1}D_m\Omega^{-1} = 0.5M_m^{-\frac{1}{2}}K_m^{-\frac{1}{2}}D_m \\ B_m &= M_m^{-1}\Phi^T B_0 \\ C_{mq} &= C_{oq}\Phi \end{aligned} \tag{5}$$

$$\Phi = [\varphi_1 \quad \varphi_2 \quad \dots \quad \varphi_n] = \begin{bmatrix} \varphi_{1n_1} & \varphi_{2n_1} & \dots & \varphi_{nn_1} \\ \varphi_{1n_2} & \varphi_{2n_2} & \dots & \varphi_{nn_2} \\ \dots & \dots & \dots & \dots \\ \varphi_{1n_k} & \varphi_{2n_k} & \dots & \varphi_{nn_k} \\ \dots & \dots & \varphi_{ij} & \dots \\ \varphi_{1n_d} & \varphi_{2n_d} & \dots & \varphi_{nn_d} \end{bmatrix},$$

The model employs the antenna node displacement q_m in the modal coordinate system as the state variable, which is transformed to the output of the antenna node displacement in natural coordinates, and it accepts the ambient load as input. The antenna’s modal mass matrix, represented by the symbol M_m , enables the modal analysis of the antenna’s finite element model to extract the modal information data for each order. Each order’s vibrational mode matrix is represented by the symbol $\psi(\varphi)$, where $\varphi_{ij}(\varphi_{ij})$ represents the displacement of the i -th order mode’s j -th degree of freedom.

The model can be used to determine how much the antenna’s main surface deforms under ambient load.

The deformation interval of the nodes on the main plane is calculated as $[y_{min}, y_{max}]$ by feeding environmental loads, such as gravity and wind load, into the dynamic model of the antenna under various operating conditions. Then, according to (1) and (3), the deformation interval of the sub-reflector, to compensate for the deformation of the main

surface, is calculated as $[\Delta d_{\min}, \Delta d_{\max}]$, where we take the maximum shape change and the minimum sub-reflector shape change as the boundary values and the sub-reflector shape adjustment limit values. The adjustment interval between the maximum value and the minimum value is fitted to form a subface shape compensation interval. This compensation interval is used as the adjustment interval for our chunked subface optimization. As the boundary values for the sub-reflector shape adjustment limit values, we use the maximum and lowest sub-reflector shape changes. A subface shape compensation interval is then formed by fitting the adjustment interval between the maximum and minimum values.

A schematic diagram of the sub-reflector compensation on the envelope surface is shown in Figure 3.

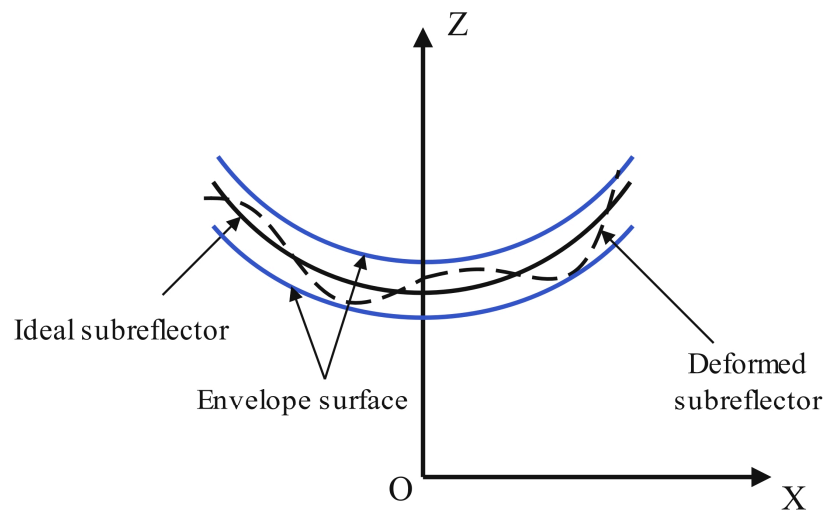


Figure 3. Sub-reflector compensation on the envelope surface.

2.3. Optimization of Sub-Reflector Array

The analysis model of the impact of the adjustment point displacement on the position of the entire panel is established based on the thin-plate bending theory in this section, which is based on the relationship between the change in the shape of the sub-reflector and the phase of the aperture field. And then, sub-reflectors are designed in blocks, and their size and quantity are optimized. Finally, a set of optimal-size and -quantity parameters are obtained. The sub-reflector is bent by utilizing an actuator to adjust the panel corner's displacement. An optimization design flow chart of the sub-reflector array size of blocks is shown in Figure 4. The panel's radial dimension is denoted by r_m . To create a sub-reflector, we arrange the trapezoidal panels in rings.

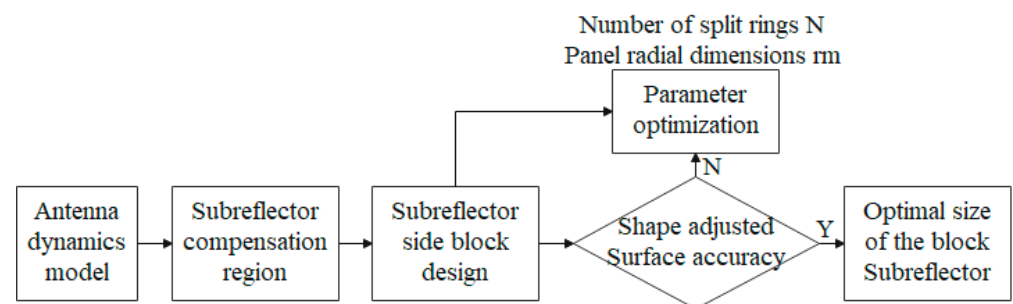


Figure 4. Sub-reflector block flow chart of antenna elevation status.

The following is the approach to optimizing the sub-reflector arrays. First, the environmental loads under different working conditions are introduced into the antenna dynamic model to calculate the deformation of the main reflector, and then the optical path difference of the aperture plane is calculated using Equation (1). Then, the optical

path difference of the opposite aperture surface is introduced into Equation (3) to obtain the compensation amount of the sub-reflector shape, and the upper and lower envelope surfaces of the sub-reflector shape adjustment are obtained by fitting these compensation amounts. Finally, the size of the sub-reflector array is optimized. With the number of sub-rings N and the radial size of the sub-reflector as the optimization variables, a set of initial values of the sub-reflector array is given, and then the genetic algorithm is used to obtain an optimal set of sub-reflector sizes.

In this paper, a trapezoidal panel is used to obstruct the sub-reflector, and the panel's four corners are used to alter the location. The sub-reflector is made up of several panels that can be modified together using one adjustment mode. A position adjustment diagram of the panel is shown in Figure 5. The shape of the sub-reflector can be changed by adjusting the position of each panel to compensate for the deformation of the main reflector.

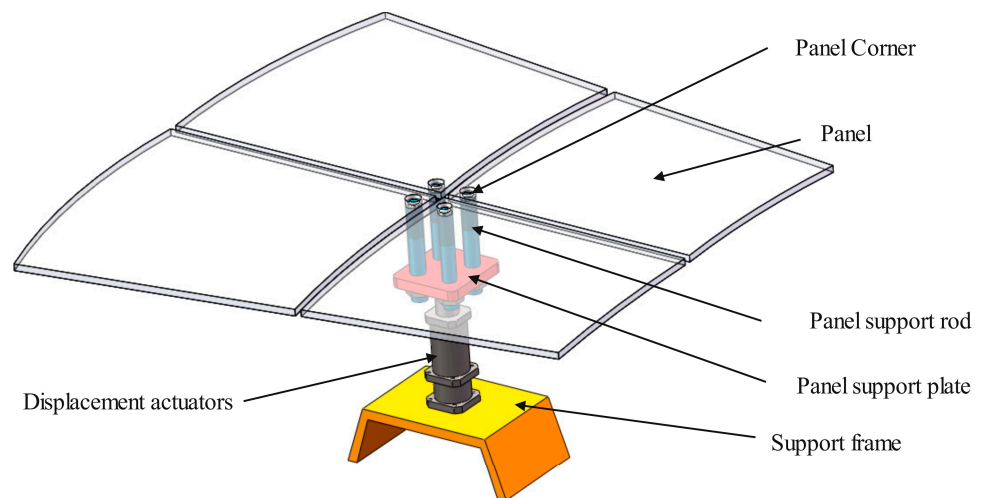


Figure 5. Schematic of panel position adjustment.

The change in four corners will cause elastic deformation of the panel, which can be simplified as simply a supported elastic thin-plate bending problem in material mechanics. The trapezoidal panel is transformed into a rectangular one, and the deflection of the rectangular panel is calculated using the thin-plate bending theory in elasticity [14], and then, converted into the deflection of the trapezoidal panel.

The trapezoidal panel is transformed into a unit square via bilinear transformation. That is, the trapezoidal panel in the (x, y) coordinates is transformed into a unit square panel in the (ξ, η) coordinates. The coordinate transformation formula is [15]:

$$\begin{cases} x_i = x(\xi_i, \eta_i) = \gamma_1 + \gamma_2\xi_i + \gamma_3\eta_i + \gamma_4\xi_i\eta_i \\ y_i = y(\xi_i, \eta_i) = \gamma_5 + \gamma_6\xi_i + \gamma_7\eta_i + \gamma_8\xi_i\eta_i \end{cases} \quad (6)$$

where (x_i, y_i) are the coordinates of the four corners of the trapezoidal panel, and (ξ_i, η_i) are the coordinates of the four corners transformed into rectangles.

The trapezoidal panel is transformed into a square panel, where $w_0 = w_0(x_i, y_i)$ is the deflection of any point (x_i, y_i) on the trapezoidal panel and $w = w(\xi_i, \eta_i)$ is the deflection of any point (ξ_i, η_i) on the square panel. According to isoparametric element theory, the deflection of corresponding points in two coordinate systems should be equal, that is, $w_0(x_i, y_i) = w(\xi_i, \eta_i)$. Therefore, the deflection at any point of the trapezoidal panel can be obtained by calculating the deflection at any point of the square panel.

If the deflection of a single panel is very tiny, the deflection can be calculated from the equilibrium differential equation of the deflection function according to the forces acting on the four corners of the panel.

According to isoparametric element theory, the bending deflection of a trapezoidal sheet is mapped to that of a unit square sheet as follows:

$$w_0 = w_0[x(\xi, \eta), y(\xi, \eta)] = \delta_1 + (\delta_2 - \delta_1)\xi + (\delta_4 - \delta_1)\eta + (\delta_1 - \delta_2 + \delta_3 - \delta_4)\xi\eta \tag{7}$$

Which is written in matrix form as follows:

$$\mathbf{W} = w_0(\mathbf{X}) = \mathbf{C}\delta \tag{8}$$

where $\mathbf{C} = \mathbf{A}^T\mathbf{R}$, and \mathbf{C} is defined as a trapezoidal sheet-bending deformation matrix, and

$$\delta = [\delta_1, \delta_2, \delta_3, \delta_4]^T, -1 \leq \xi \leq 1, -1 \leq \eta \leq 1, \mathbf{R} = \begin{bmatrix} 1 & 0 & 0 & 0 \\ -1 & 1 & 0 & 0 \\ -1 & 0 & 0 & 1 \\ 1 & -1 & 1 & -1 \end{bmatrix}.$$

According to Equations (6) and (8), the deformation of a single panel can be obtained using the coordinates and the normal displacement of adjusting corners.

The whole panel is made up of several panels. One actuator is employed at each corner of the panel overlap to share the adjustment of the position of the four corners by the electric cylinder.

Assume that the whole sub-reflector has N panels, which are adjusted by h actuators. Then, the reflecting surface deformation matrix $\tilde{\mathbf{C}}$ can be divided into N sparse matrices, as shown in Figure 6. Then, the deformation distribution of the entire reflecting surface is as follows:

$$\mathbf{W}_{\text{all}} = \tilde{\mathbf{C}}\delta_{\text{all}} = \begin{bmatrix} \tilde{\mathbf{C}}_1 & & & \\ & \tilde{\mathbf{C}}_2 & & \\ & & \ddots & \\ & & & \tilde{\mathbf{C}}_N \end{bmatrix} \begin{bmatrix} \delta_1 \\ \delta_2 \\ \vdots \\ \delta_h \end{bmatrix} \tag{9}$$

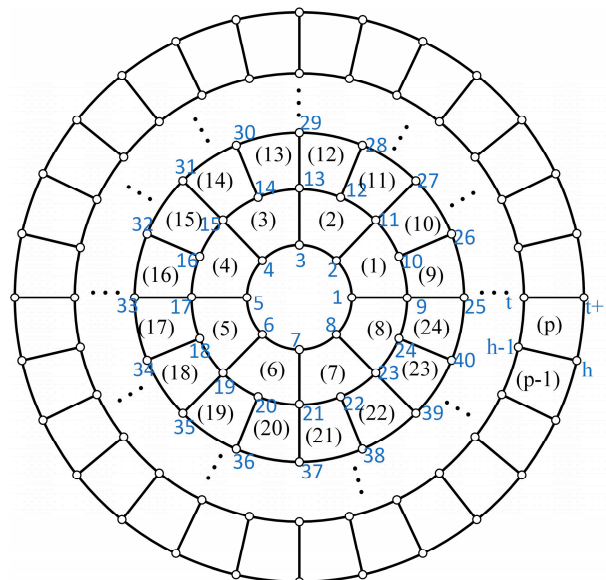


Figure 6. A sketch of the distribution of the reflector structure with the shared adjustment.

For the sub-reflector array problem, to ensure that panels share one adjusting cylinder, a set of initial block size values are given before optimization.

The objective function is taken to be the Root Mean Square Error (RMS) between the z-direction variation of the sub-reflector and the variation in the targets between the envelope surfaces. The variables for optimization are the number of ring segments and

the radial size of each ring. The RMS value of the objective function is based on the size accuracy of the antenna sub-reflector. The optimization model of the sub-reflector size is established as follows:

$$\begin{aligned}
 &\text{Find } X = (r_1, r_2, \dots, r_N, N)^T \\
 &\text{Min } \text{RMS} = \sqrt{\left(\sum_{i=1}^n (\Delta z_i - \Delta z_i^l)^2\right) / n} \\
 &\text{S.t. } 0 < r_i \leq r_{i+1} \\
 &\quad S_i \leq S_{\max}
 \end{aligned} \tag{10}$$

where r_i is the radius of each ring N is the ring-dividing number, S_i is the area of each panel, S_{\max} is the maximum area of the panel related to machining accuracy, Δz_i^l is the distance between two envelope surfaces in the z direction, and Δz_i is the change in the z direction of the sub-reflector shape.

3. Electrical Performance Method of Sub-Reflector Array

The antenna will be affected by the environmental load in the operational environment, resulting in reflector distortion and antenna aperture field distortion. The antenna gain can be reduced, and the beam direction can be deflected as a result of this issue. Firstly, an electromechanical coupling model is established to analyze the influence of reflector deformation on the antenna’s electrical performance, and then, the shape change and position change of the block side face used to compensate for the electrical performance are calculated. Finally, the shape of the sub-reflector and the change in position are introduced to examine the compensatory impact of the deformation antenna. A flow chart of the electrical performance compensation is given in Figure 7:

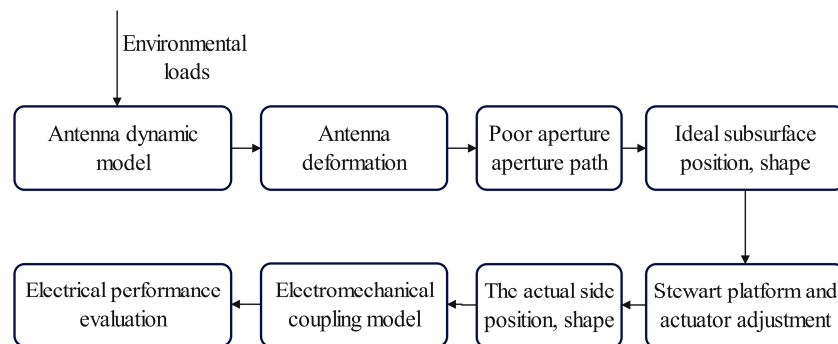


Figure 7. A flow chart of electrical performance compensation.

3.1. Electromechanical Coupling Model of Dual-Reflector Antenna

Neither the sub-reflector array adjustment approach nor the decrease in antenna performance caused by reflector deformation can be accurately analyzed using the current electromagnetic simulation tools. A bi-reflective electromechanical coupling model is therefore created using the PO/PO method, and the procedure is as follows: the reflector model is established, the reflector is divided into triangular elements for electromagnetic calculation, and then, we calculate the Gauss integration points from the triangular elements, as well as the surface current from the feed to each integration point on the sub-reflector. Following this, the area of the triangular element corresponding to each integral point on the principal plane is cross-multiplied using the near-field formula to determine the magnetic field radiated by the induced current at each integral point on the sub-reflector to each integral point on the principal plane. Finally, using the PO approach and the main surface as the origin, the far field of the main surface radiation is determined. The modeling process is as follows:

As shown in Figure 8, the phase center of the feed is taken as the phase reference point. Assuming the power direction function of the feed is $G_f(\xi, \phi')$, the incident electric field E_i can be expressed using the following formula [16]:

$$E_i = \left[\sqrt{\frac{\mu_0}{\epsilon_0}} \frac{P_t}{4\pi} \right]^{1/2} \sqrt{G_f(\xi, \phi')} \frac{e^{-jkr'}}{r'} \hat{e}_i \tag{11}$$

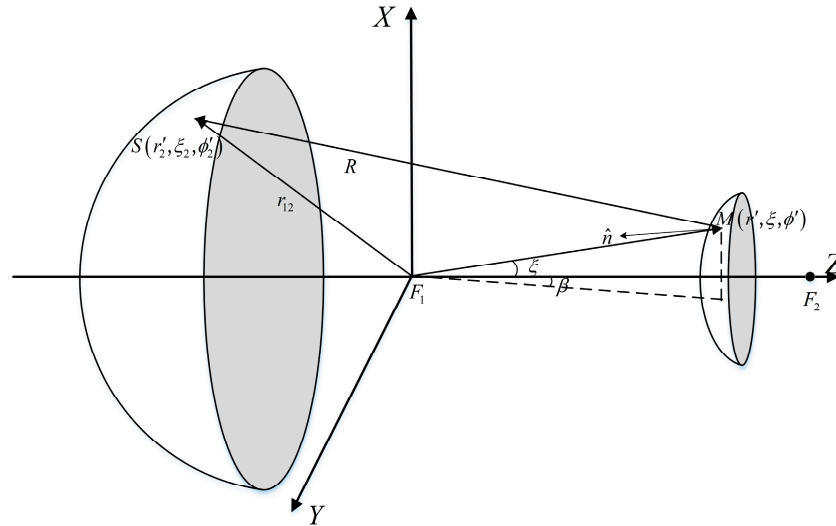


Figure 8. Feed to sub-reflector diagram.

The electromagnetic wave emitted by the feed will produce a magnetic field H_i when it hits the reflector, which can be calculated using the incident electric field E_i . Since the reflector is in the far field of the feed,

$$H_i = \sqrt{\frac{\epsilon_0}{\mu_0}} \left(\hat{r}_0' \times E_i \right) \tag{12}$$

where \hat{r}_0' is the unit vector in the direction r' of the vector diameter. The current density vector of the reflector can be obtained as follows:

$$J_s^e = 2\hat{n} \times H_i \tag{13}$$

By introducing (11) and (12) into (13), the surface current density of M at any point on the paraboloid is obtained:

$$J_s^e = \left[4\sqrt{\frac{\epsilon_0}{\mu_0}} \frac{P_t}{4\pi} \right]^{1/2} \left[\hat{n} \times \left(\hat{r}_0' \times \hat{e}_i \right) \right] \times \sqrt{G_f(\xi, \phi')} \frac{e^{-jkr'}}{r'} \hat{e}_i \tag{14}$$

where $C = \left[4\sqrt{\frac{\epsilon_0}{\mu_0}} \frac{P_t}{4\pi} \right]^{1/2}$ is a constant related to the power of the feed. \hat{e}_i is the unit vector of the polarization direction of the incident field, which can be decomposed into three components of the rectangular coordinate system.

$$\hat{e}_{ix} = \hat{x}_0 (\cos \xi \cos^2 \phi' + \sin^2 \phi') + \hat{y}_0 (\cos \xi \sin \phi' \cos \phi' - \sin \phi' \cos \phi') - \hat{z}_0 (\sin \xi \cos \phi') \tag{15}$$

in which \hat{n} is the normal unit vector of the vector on the reflector, which can be decomposed into x, y, z axes: $n_x = -\sin(\xi/2) \cos \phi'$, $n_y = -\sin(\xi/2) \sin \phi'$, $n_z = \cos(\xi/2)$.

Then, we can calculate the magnetic field reflected from the sub-reflector to the main reflector [17] as:

$$\begin{aligned} H_m &= \iint J_s^e \times \nabla' g \, ds \\ &= \frac{1}{4\pi} \iint \frac{e^{-jkr_m}}{r_m} (J_s^e \times r_m) \left(jk + \frac{1}{r_m} \right) ds \end{aligned} \tag{16}$$

where \hat{N} is the surface current density at each integration point on the sub-reflector, r_m is the distance from each Gaussian integration point on the sub-reflector to the Gauss integration point on the primary surface, and ds is the area element on the sub-reflector. The magnetic field from each integral point of the sub-reflector to each integral point of the main surface is calculated, and then, the total magnetic field H_m generated by the main surface is obtained via summation. The far field of radiation generated by the main surface is then calculated from the focal point F_2 of the main surface, as shown in Figure 9.

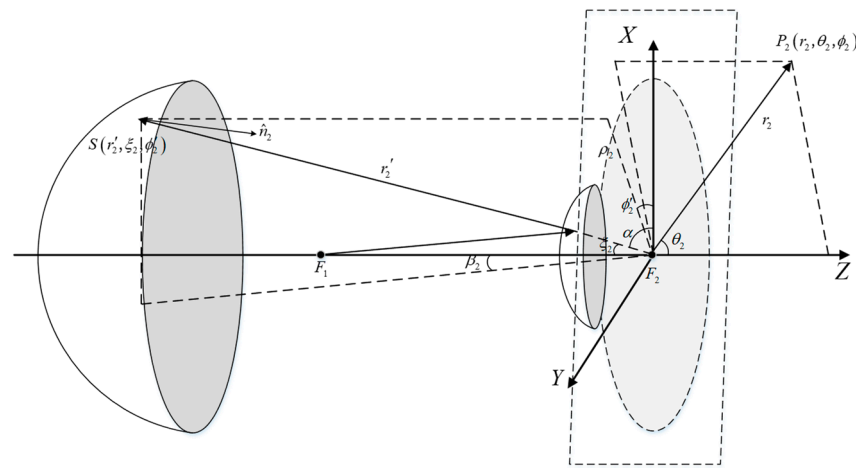


Figure 9. Coordinate relationship diagram from the sub-reflector to the main reflector.

The normal vector \hat{n}_2 of each element on the main reflector is calculated, and the current density on the main reflector is calculated according to (13):

$$J_m^e = 2 \left(H_m \times \hat{n}_2 \right) \tag{17}$$

Considering only the radiation of the current density x component J_{xm}^e on the main surface, $J_m^e = \hat{x}_0 J_{xm}^e$. The far-field electric field values on the main surface can be calculated as follows:

$$E_2 = -\frac{j60\pi}{\lambda r_2} e^{-jkr} \int_{S_2} J_{xs}^e e^{jkr_2 \cdot \hat{r}_{02}} ds \tag{18}$$

Convert (18) to polar coordinates and consider the direction of the coordinates:

$$\begin{aligned} E_{2\theta} &= -\frac{j60\pi}{\lambda r_2} e^{-jkr_2} \\ &\times \int_{S_2} J_{xm}^e e^{jkr_2' (\sin\theta_2 \sin\xi_2 \cos(\phi_2 - \phi_2') - \cos(\xi_2) \cos\theta)} ds \end{aligned} \tag{19}$$

3.2. Calculation of Compensation

Once the electromechanical coupling model of the dual-reflector antennas has been established, the adjustment of the position and shape of the sub-reflector is calculated.

3.2.1. Sub-Reflector Form and Posture Adjustment

The form and posture of the antenna sub-reflector will cause beam deflection, so changing the sub-reflector position can compensate for the pointing error caused by antenna

deformation. In this section, according to the best fitting paraboloid theory, six deformation parameters of the deformation paraboloid relative to the ideal paraboloid are calculated by fitting the best-fitting paraboloid, namely, du , dv , dw , ϕ_u , ϕ_v , and df . We can use the following formula to calculate the optimal vertex position of the sub-reflector:

$$\begin{cases} x_s = \Delta x + (f_0 + \Delta f)\phi_y \\ y_s = \Delta y - (f_0 + \Delta f)\phi_x \\ z_s = f_0 + \Delta f + \Delta z \end{cases} \quad (20)$$

The optimal position diagram of the sub-reflector is shown in Figure 10.

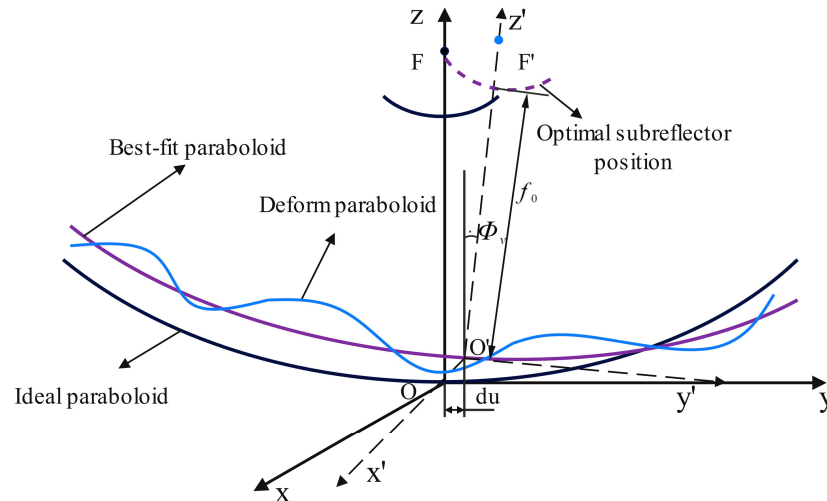


Figure 10. The optimal position of the sub-reflector.

The values of the pointing deviation and the gain loss are derived by incorporating the deformation data of the deformed reflector into the electromechanical coupling model developed in the previous section. The best sub-reflector position is obtained using the best-fitting paraboloid and (20) of the deformed paraboloid, and the form and posture of the sub-reflector are changed to the best. By incorporating the displacement into the electromechanical coupling model, the viability of compensating for the sub-reflector’s electrical performance is confirmed.

3.2.2. Sub-Reflector Shape Adjustment

Using (1), one may determine the optical path difference brought on by wind load, and then, one can use (3) to compute the optimal sub-reflector’s shape modification. An active sub-reflector adjustment method [18] is used to account for the optical path difference of the aperture surface caused by antenna deformation. Its basic theory is to take into account the elastic deformation of the panel caused by adjusting the corner displacement of a single panel and the change in the optical path difference of the aperture surface caused by all the adjustment point displacements of the entire sub-reflector. The objective is to minimize the surface error after the active adjustment of the sub-reflector array shape and to obtain the best adjustment value of each adjustment point. Suppose the adjusted error is:

$$V = W_0 + \Delta W = W_0 + \tilde{C}\delta_{all} \quad (21)$$

where W_0 is the initial shape matrix of the shape surface ΔW is the change in the sub-reflector caused by the adjustment. According to the least squares principle:

$$\sum v_i^2 = \sum (w_{0,i} + \Delta w_i)^2 = \min \quad (22)$$

Convert the superposition into a matrix form:

$$V^T V = \left(W_0 + \tilde{C} \delta_{\text{all}} \right)^T \left(W_0 + \tilde{C} \delta_{\text{all}} \right) = \min \quad (23)$$

The above equation is solved according to the normal equation solution method of least squares; then, the solution of the equation is:

$$\delta_{\text{all}} = - \left(\tilde{C}^T \tilde{C} \right)^{-1} \tilde{C}^T W_0 = S \cdot W_0 \quad (24)$$

Then, (24) is the adjustment quantity with the minimum error of the sub-reflector, in which S is the sub-reflector adjustment matrix.

W_0 is the initial form-face accuracy matrix, and the one that follows is the amount of shape change. In Equation (21), V represents the form-face accuracy matrix following the sub-reflector's shape adjustment. To obtain the corrected form-face accuracy, the two are summed together. For the purpose of computing least squares, each member of the matrix in Equation (21) is squared in Equation (22). Equation (22) is expressed as a matrix multiplication in Equation (23). Equation (24) is analytically solved and compacted to yield the actuator-by-actuator adjustment.

After calculating the adjustment of each actuator, the actual deformation of the sub-reflector can be obtained by substituting the (12). The calculated deformation of the sub-reflector is put into the double inverse electromechanical coupling model with the main reflector deformation. Finally, a far-field direction diagram is obtained.

4. Example Analysis

4.1. Optimization Result of Sub-Reflector Array

This part concludes the confirmation of the compensating effect, as well as the optimization design of the sub-reflector structure, taking the 65 m antenna as an example. The 65 m antenna structure is shown in Figure 11. The direction of the black arrow is the wind direction as shown in Figure 11. The 65 m antenna weighs 2640 t. A wind load with an average wind speed of 12 m/s is applied to the reflector. The equivalent wind force is applied to each node of the reflector on average, that is, the wind force is brought into the antenna dynamics model (4), and the deformation information of each node of the antenna reflector is obtained.

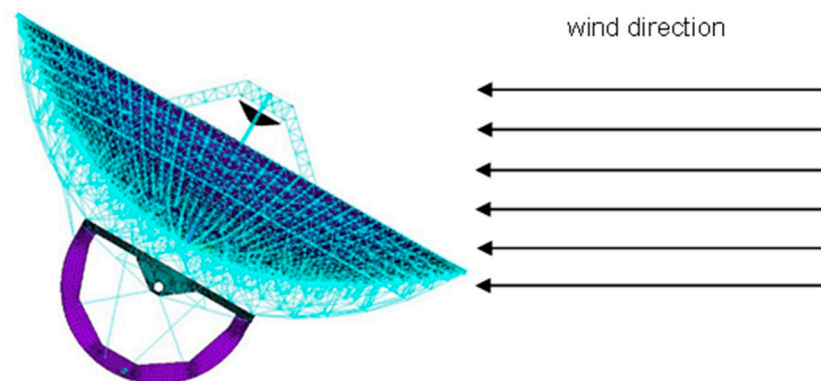


Figure 11. Finite element model of 65 m antenna.

The deformation of the reflector antenna at the maximum and minimum wind force is substituted into Equation (1) to obtain the optical path difference of the antenna aperture surface, as shown in Figure 12.

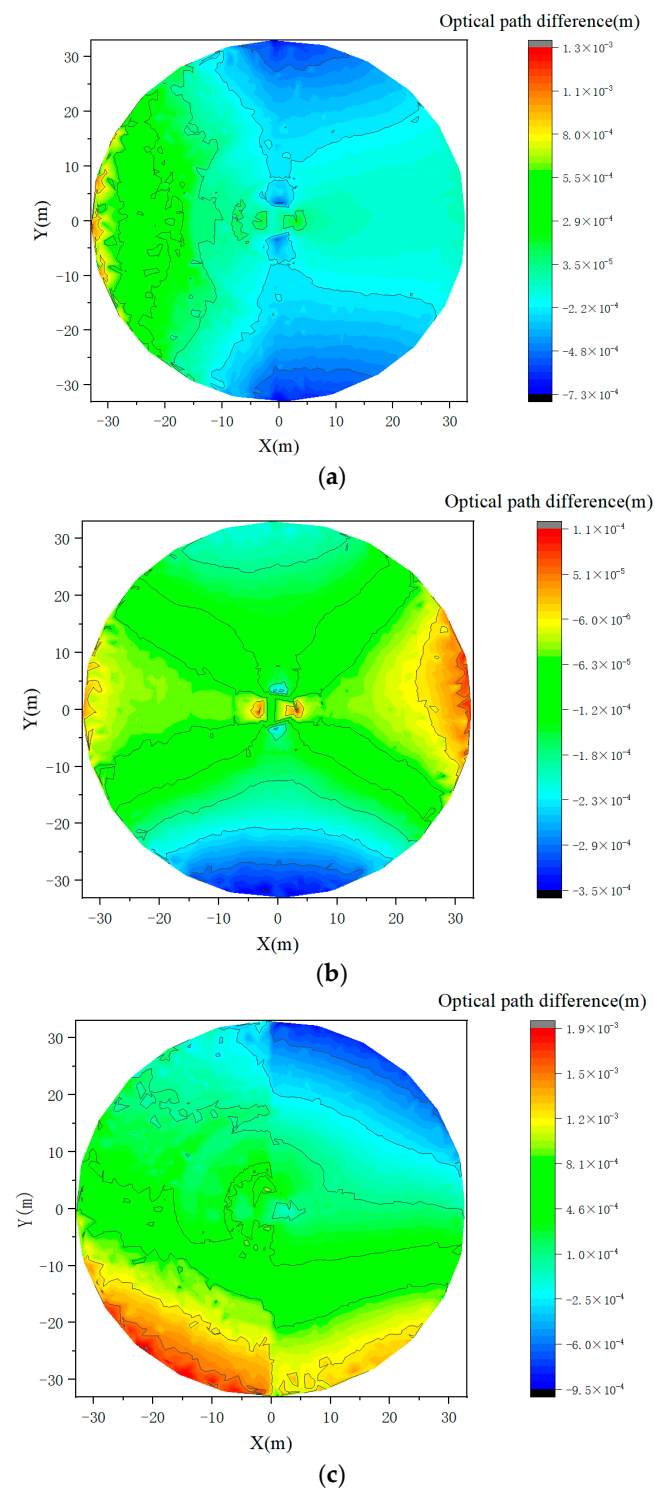


Figure 12. Optical path difference of aperture surface caused by wind disturbance. (a) Aperture optical path difference at maximum wind at 90° ; (b) aperture optical path difference at minimum wind at 90° ; (c) aperture optical path difference at maximum wind at 45° .

The dynamic model of the 65 m antenna is also used to apply gravity load to the antenna under different pitching conditions, and the deformation information of each node of the antenna reflector is calculated. Then, the optical path difference of the aperture surface is obtained using Equation (1), as shown in Figure 13.

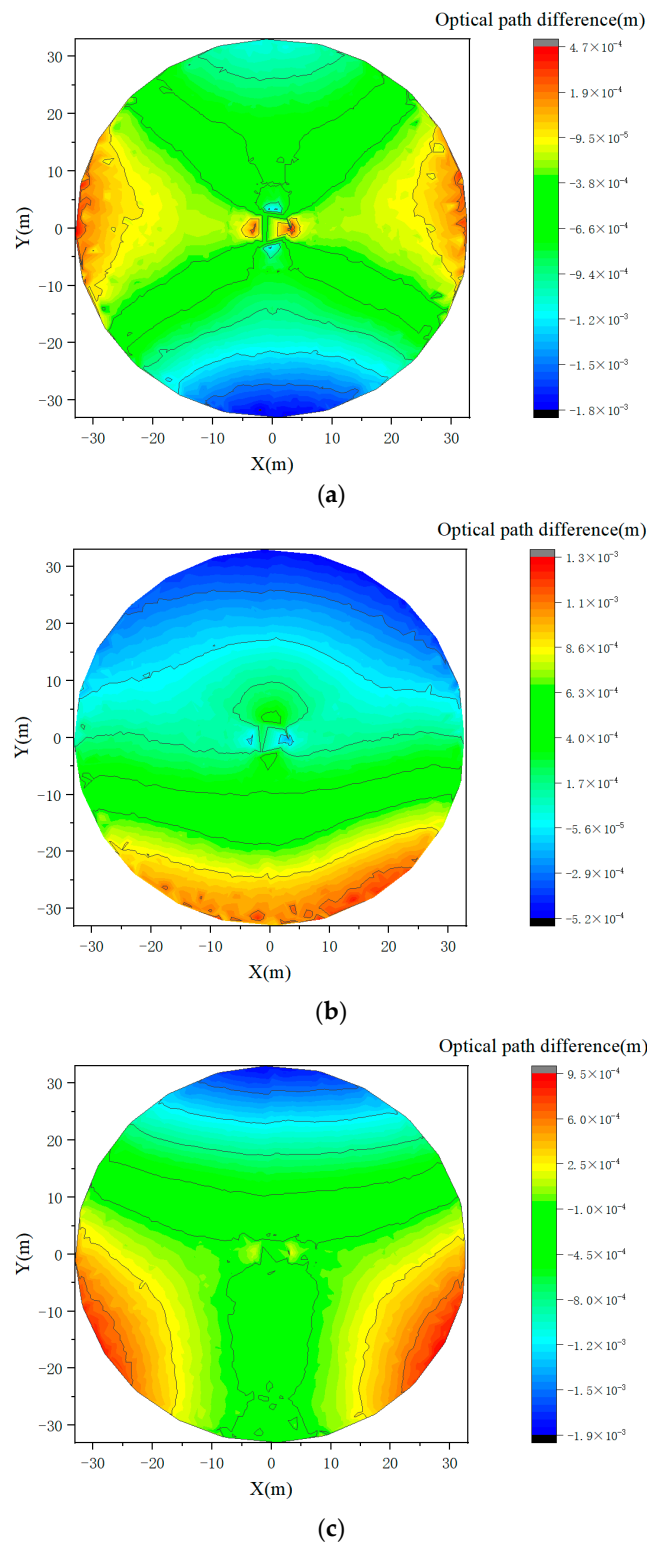


Figure 13. Optical path difference of aperture surface caused by gravity. (a) Optical path difference of aperture surface at 90°; (b) optical path difference of aperture surface at 45°; (c) optical path difference of aperture surface at 0°.

The size accuracy of the 65 m antenna sub-reflector is required to be 0.05 mm for the size of a single panel. But the size accuracy of a single panel is related to its size (the larger the size, the lower the accuracy), and the maximum panel area cannot exceed 2 m² to meet the accuracy requirements of a single panel. For the whole sub-reflector, the size accuracy

of the 65 m antenna is required to be 0.07 mm [19]. In order to achieve the requirements, the dimensional accuracy of the sub-facets is optimized based on this accuracy requirement.

The genetic algorithm is used to optimize the size of the sub-reflector, and the optical path difference of the antenna aperture caused by the environmental load is calculated from Figures 12 and 13. According to Equation (3), the minimum adjustment value of under different environmental loads is calculated. Finally, the sub-reflector minimum adjustment value of the sub-reflector under different environmental loads is combined to obtain the envelope of the deformed sub-reflector under different environmental loads. The calculated results show that the adjustment compensation interval is [1.1 mm, 4.62 mm]. As shown in Figure 3, the minimum adjustment range of the profile position is specified as the space between the two envelopes.

According to the optimization model established using (14), the size parameters of the sub-reflector are optimized using a genetic optimization algorithm. The number of rings N is optimized in the case of the two, the three, and the four rings, respectively. The results show that the fitting error of $N = 2$ is 0.0916 mm, which does not meet the requirement. The fitting accuracy of $N = 3$ is 0.0648 mm, and that of $N = 4$ is 0.053 mm. The fitting accuracy of $N = 3$ and $N = 4$ meets the requirement. As $N = 3$ uses fewer panels and meets the accuracy requirements, three is selected as the final optimization result. The iteration curve for three is shown in Figure 14.

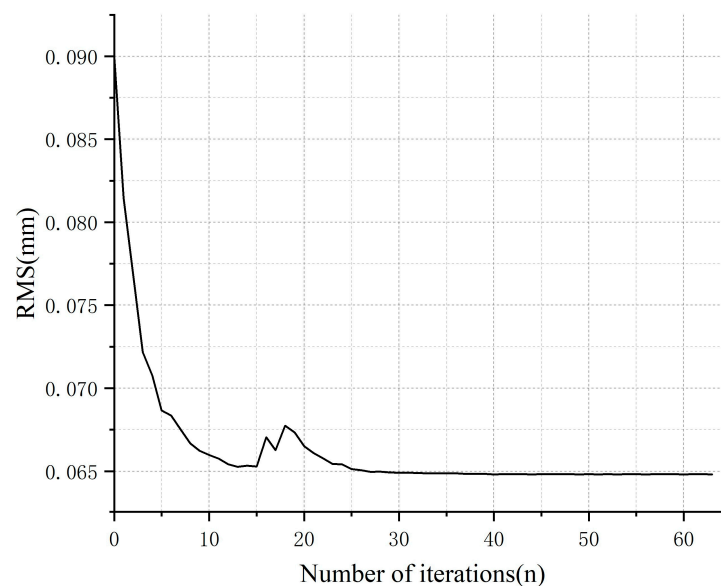


Figure 14. Optimized iteration curve.

In the iterative process of calculating the dimensions of each panel of the sub-reflector, the optimization algorithm's iterative curve is obtained, and is depicted in Figure 14. The vertical axis represents the form-face accuracy computed for the sub-reflector dimensions used during each iteration, while the horizontal axis represents the number of iterations. The form-face accuracy must drop to the accuracy requirement value, or 0.07 mm, in order for the iteration to end.

Following optimization, an overall structure diagram of the sub-reflector is shown in Figure 15, which consists of 40 trapezoidal panels and 1 circular panel. The blue number indicates the number of actuators used. One electric cylinder, out of a total of fifty-six, is utilized in the shared adjustment mode to control the position change of several panels.

The size parameters obtained after genetic algorithm optimization are shown in Table 1.

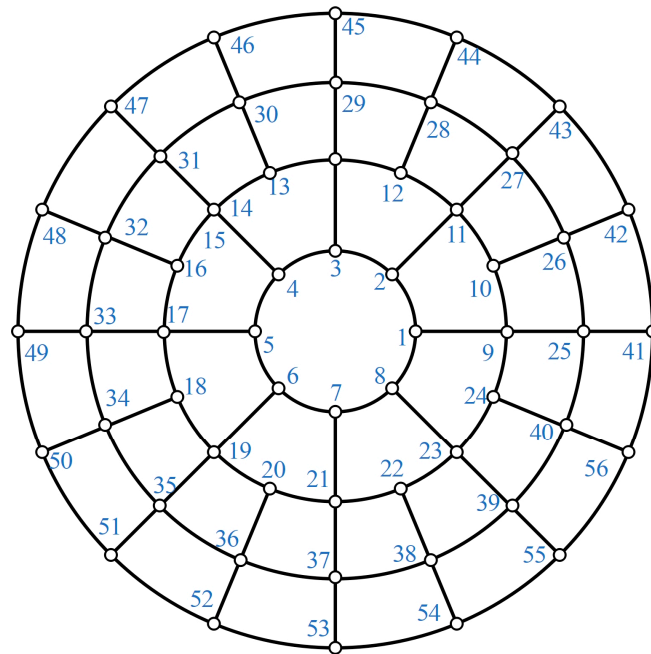


Figure 15. Schematic diagram of sub-reflector optimization structure.

Table 1. Radial dimensions of each panel.

Number of Rings (N)	R1 (m)	R2 (m)	R3 (m)	R4 (m)
3	0.772	1.644	2.386	3.05

4.2. Adjustment of Sub-Reflector Array

Taking the deformation shown in Figure 12 caused by maximum wind load at 90 degrees as an example, according to the optical path difference data of the aperture surface and Equation (3), the ideal adjustment amount of the sub-reflector array is calculated as shown in Figure 16.

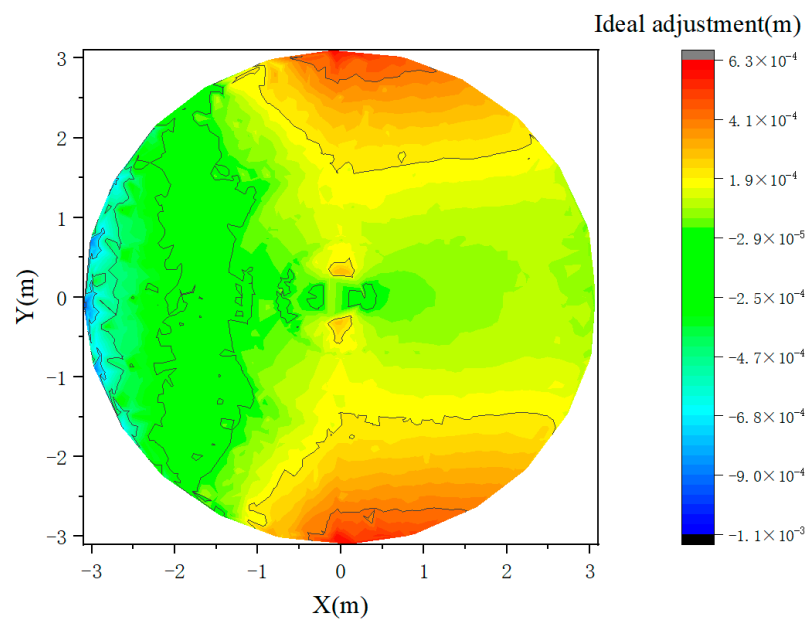


Figure 16. Ideal adjustment of sub-reflector array.

The electric cylinder adjusts the sub-reflector as a whole. Due to the limited installation space and the sub-reflector’s adjustment range of 0 to 10 mm, the micro-electric cylinder of model T506-BK is employed. Its electric cylinder stroke is 30 mm, positioning accuracy is 0.01 mm, rated thrust is 64 N, and maximum speed is 12 mm/s. A position loop bandwidth of 7.4 Hz was computed using the position loop control model.

Then, according to Equation (24), the best adjustment quantity of four corners of each panel is calculated, and the partial adjustment quantity of each electric cylinder of the actuators is shown in Table 2.

Table 2. Adjustment of each electric cylinder.

Actuator Number	Adjustment Amount (mm)	Actuator Number	Adjustment Amount (mm)
1	0.161	47	0.101
2	0.081	48	0.081
3	0.102	49	0.149
4	0.114	50	0.127
5	0.102	51	0.106
6	0.108	52	0.084
7	0.113	53	0.158
8	0.118	54	0.134
9	0.101	55	0.111
10	0.109	56	0.087
⋮	⋮		

According to (8), the actual deformation of each panel on the sub-reflector array is calculated, as shown in Figure 17. The RMS of the theoretical and actual sub-reflector shapes is 0.0508 mm.

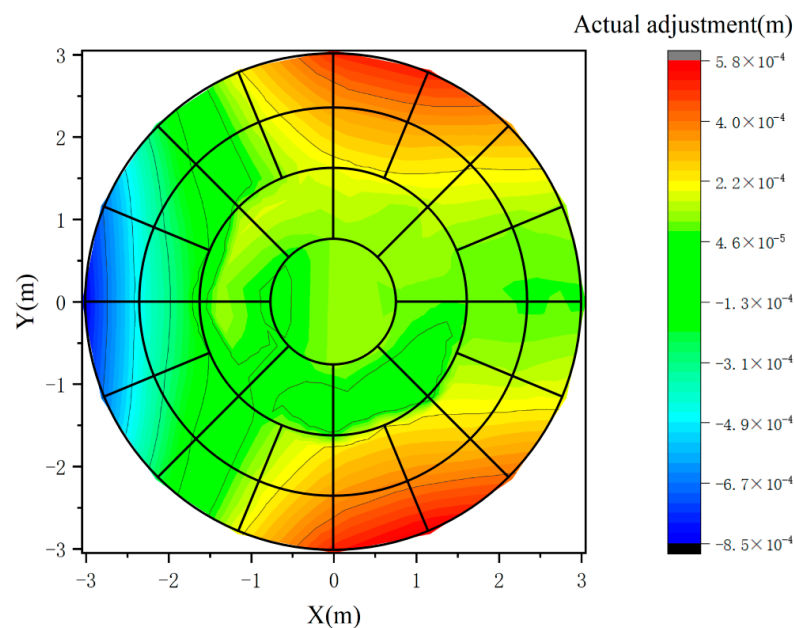


Figure 17. Deformation of sub-reflector array.

Table 3 presents a comparison of the accuracy of the main face shape adjustment utilized in this paper, the flexible sub-facial shape adjustment, and the chunked negative shape adjustment approach.

Table 3. Adjustment accuracy comparison.

Compensation Method	Root mean square error (RMS) (mm)
Main Face Compensation	0.24
Flexible Sub-Face Compensation	0.1438
Block Sub-Face Compensation	0.0508

4.3. Sub-Reflector Position Adjustment Amount

Using the best paraboloid fitting theory, the six deformation parameters between the best-matched paraboloid and the ideal are calculated, as shown in Table 4.

Table 4. Paraboloid deformation parameters.

Freedom	du	dv	dw	df
Variation (m)	4.37×10^{-5}	1.76×10^{-6}	1.67×10^{-4}	1.07×10^{-5}
Freedom	φ_u	φ_v		
Variation ($^\circ$)	6.86×10^{-5}	1.70×10^{-3}		

According to Equation (20) and the six deformation parameters calculated in Table 4, the optimal vertex position of the sub-reflector is calculated as $(5.72 \times 10^{-4}, 2.31 \times 10^{-5}, 17.8052)$, and the sub-reflector is moved to the optimal position to carry out the position compensation.

To change the form and posture of the sub-reflector, we use a Stewart platform. This consists of a moving platform, a stationary platform, and six electric cylinders. The electric cylinder is connected to the higher and lower platforms, the mobile platform is attached to the sub-reflector-supporting truss, and the static platform is connected to the auxiliary supporting leg of the auxiliary supporting surface. The electric cylinder employs a big precision electric cylinder with a model number of GF17XL-SH-20-850, rated thrust of 339 N, 1700 mm stroke, positioning accuracy of 0.02 mm, and maximum speed of 1200 mm/s. The Stewart platform has six degrees of freedom for movement. The Stewart platform's servo bandwidth of the platform's translational freedom is determined to be 1.942 Hz by building dynamic and kinematic models of the platform. The antenna aiming error spectrum analysis result is 90 under 1.9 Hz, which satisfies the compensation system's requirements.

A compensated far-field pattern is obtained by introducing the distorted sub-reflector shape and the change in the sub-reflector's form and posture into the electromechanical coupling model. The comparison of the far-field pattern of the antenna before and after using the shape adjustment of the sub-reflector and the attitude compensation of the sub-reflector is shown in Figure 18. According to the shape of the pattern in Figure 18, the gain of the 65 m antenna decreases by 0.44315 dB after adding wind load, resulting in a pointing error of 0.00143° . After sub-reflector compensation, the gain is increased by 0.36287 dB and the pointing error is reduced to 0.00047° .

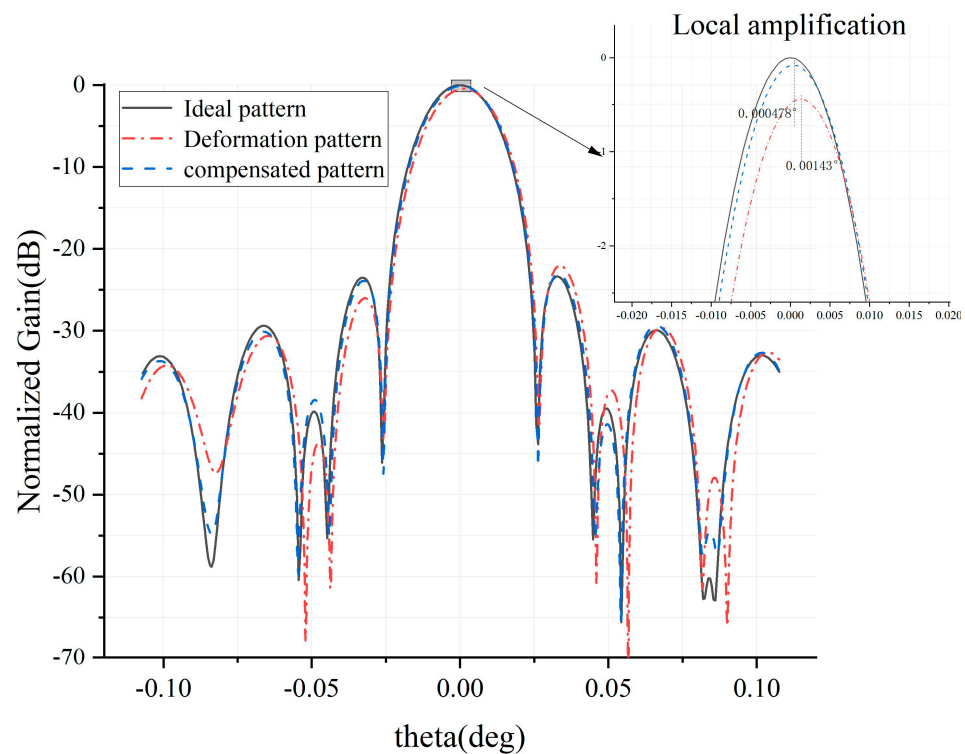


Figure 18. The antenna pattern before and after sub-reflector array compensation.

5. Conclusions

In this paper, the deformation of the antenna brought on by environmental factors, such as wind load, is solved using a sub-reflector array technique. The sub-reflector is designed in blocks, and the whole sub-reflector is deformed by moving the position of each panel to compensate for the optical path difference of the antenna aperture surface caused by environmental load. The example's outcome demonstrates that the sub-reflector array shape adjustment method reduces gain error by 84 percent and lowers aiming error by 67 percent. This is a promising compensation method.

Author Contributions: Conceptualization, J.Z.; Methodology, J.Z.; Software, X.K.; Validation, X.K.; Formal analysis, J.Z.; Data curation, C.Z.; Writing—original draft, Y.G. and Q.H.; Writing—review & editing, C.Z. All authors have read and agreed to the published version of the manuscript.

Funding: This work was supported in part by the National Natural Science Foundation of China under Grant 52035010 and 52275372, in part by Shaanxi Innovation Team Project under Grant 2018TD-012, in part by Shaanxi Key Industry Chain Project under Grant 2020ZDLGY14-08, and in part by the National 111 Project under Grant B14042, in part by Natural Science Basic Research Program of Shaanxi under Grant 2023-JC-YB-320.

Data Availability Statement: The data of this article is unavailable due to privacy.

Conflicts of Interest: The authors declare no conflict of interest.

References

1. Wang, C.S.; Xiao, L.; Wang, W.; Xu, Q.; Xiang, B.B.; Zhong, J.F.; Jiang, L.; Bao, H.; Wang, N. An adjustment method for active reflector of large high-frequency antennas considering gain and boresight. *Res. Astron. Astrophys.* **2017**, *17*, 41–52. [[CrossRef](#)]
2. Li, P.; Duan, B.Y.; Wang, W.; Zheng, F. Electromechanical Coupling Analysis of Ground Reflector Antennas under Solar Radiation. *IEEE Antennas Propag. Mag.* **2012**, *54*, 40–57. [[CrossRef](#)]
3. Wang, C.S.; Wang, W.; Song, L.W. *Microwave Antenna Multi Field Coupling Theory and Technology*; Science Press: Beijing, China, 2015. (In Chinese)
4. Lacasse, R.J. Green Bank Telescope active surface system. In *Green: Proceedings of Astronomical Telescopes and Instrumentation*; International Society for Optics and Photonics: Bellingham, WA, USA, 1998.

5. Gawronski, W. Control and Pointing Challenges of Large Antennas and Telescopes. *IEEE Trans. Control Syst. Technol.* **2007**, *15*, 276–289. [[CrossRef](#)]
6. Zhang, J.; Huang, J.; Zhou, J.; Wang, C.; Zhu, Y. A Compensator for Large Antennas Based on Pointing Error Estimation under a Wind Load. *IEEE Trans. Control Syst. Technol.* **2017**, *25*, 1912–1920. [[CrossRef](#)]
7. Zhang, J.; Huang, J.; Wang, S.; Wang, C. An Active Pointing Compensator for Large Beam Waveguide Antenna Under Wind Disturbance. *IEEE/ASME Trans. Mechatron.* **2015**, *21*, 860–871. [[CrossRef](#)]
8. Leng, G.J.; Wang, W.; Duan, B.Y.; Li, X.P. Sub-reflector real-time compensation for main reflector deformation of shaped Cassegrain antenna. *Syst. Eng. Electron. Technol.* **2011**, *33*, 996–1000. (In Chinese)
9. Ban, Y.; Wang, C.; Feng, S.; Duan, B.; Wang, W. Iteration Path-Length Error Correction Approach to Sub-reflector Shaping for Distortion Compensation of Large Reflector Antenna. *IEEE Trans. Antennas Propag.* **2019**, *67*, 2729–2734. [[CrossRef](#)]
10. Huang, J.; Encinar, J.A. *Reflectarray Antennas*; IEEE Press: New York, NY, USA, 2008.
11. Xu, S.; Rahmat-Samii, Y.; Imbriale, W.A. Subreflectarrays for Reflector Surface Distortion Compensation. *IEEE Trans. Antennas Propag.* **2009**, *57*, 364–372. [[CrossRef](#)]
12. Xiang, B.; Zheng, T.; Wang, W.; Lian, P.; Kazezkhan, G.; Zhou, J.; Li, K. Active Adjustment of the Subreflector Shape for the Large Dual-Reflector Antenna. *Micromachines* **2023**, *14*, 1893. [[CrossRef](#)] [[PubMed](#)]
13. Zhang, J.; Huang, J.; Qiu, L.; Song, R. Analysis of Reflector Vibration-Induced Pointing Errors for Large Antennas Subject to Wind Disturbance: Evaluating the pointing error caused by reflector deformation. *IEEE Antennas Propag. Mag.* **2015**, *57*, 46–61. [[CrossRef](#)]
14. Ye, S.; Duan, B. A Unified Approach of Structural Optimization on Geometrical Configuration and Member Sizing of Antenna Structure. *Comput. Struct. Mech. Appl.* **1986**, *3*, 57–65. (In Chinese)
15. Chen, J.; Li, L.; Long, S. Solving the Bending Problem of Arbitrary Quadrilateral Plates by Generalized Kantorovich Method. *Eng. Mech.* **1991**, *8*, 59–72. (In Chinese)
16. Wei, W. *Antenna Principle*; National Defense Industry Press: Arlington, VA, USA, 1985.
17. Xu, H.; Heng, Y.; Shang, Y.; Xia, L. A Fast Computing Method for Dual Reflector Antennas. *Guid. Fuze* **2018**, *2*, 42–45.
18. Lian, P.; Wang, C.; Xue, S.; Xu, Q.; Wang, N.; Xiang, B.; Shi, Y.; Jia, Y. Panel Adjustment and Error Analysis for a Large Active Main Reflector Antenna by Using the Panel Adjustment Matrix. *IEEE Trans. Antennas Propag.* **2021**, *69*, 6351–6363. [[CrossRef](#)]
19. Liu, G.; Zheng, Y. *Antenna Design of Shanghai 65 m Radio Telescope*; The 54th Research Institute of China Electronics Technology Corporation: Shijiazhuang, China, 2009.

Disclaimer/Publisher’s Note: The statements, opinions and data contained in all publications are solely those of the individual author(s) and contributor(s) and not of MDPI and/or the editor(s). MDPI and/or the editor(s) disclaim responsibility for any injury to people or property resulting from any ideas, methods, instructions or products referred to in the content.